

# Convection in a rapidly rotating spherical shell with an imposed laterally varying thermal boundary condition

Christopher J. Davies<sup>1</sup>, David Gubbins<sup>1</sup> AND Peter K. Jimack<sup>2</sup>

<sup>1</sup>School of Earth and Environment, University of Leeds, Leeds LS2 9JT, UK.

<sup>2</sup>School of Computing, University of Leeds, Leeds LS2 9JT, UK.

(Received )

We investigate thermally-driven convection in a rotating spherical shell subject to inhomogeneous heating on the outer boundary, extending previous results to more rapid rotation rates and larger amplitudes of the boundary heating. The analysis explores the conditions under which steady flows can be obtained, and the stability of these solutions, for two boundary heating modes: first, when the scale of the boundary heating corresponds to the most unstable mode of the homogeneous problem; second, when the scale is larger. In the former case stable steady solutions exhibit a two-layer flow pattern at moderate rotation rates, but at very rapid rotation rates no steady solutions exist. In the latter case, stable steady solutions are always possible, and unstable solutions show convection rolls that cluster into nests that are out of phase with the boundary anomalies and remain trapped for many thermal diffusion times.

---

## 1. Introduction

The problem of thermally-driven convection in a rapidly rotating spherical shell with homogeneous boundary conditions (Chandrasekhar 1961) has been extensively studied owing to its application to planetary cores. The governing nondimensional parameters are defined in full in equation 2.4 below; they are the Rayleigh number,  $R$ , measuring the strength of the applied temperature difference across the shell, the Ekman number,  $E$ , measuring the rate of rotation, and the Prandtl number,  $Pr$ , the ratio of viscous and thermal diffusivities. Initial work on this problem, herein called the *homogeneous problem*, focused on the onset of convective instability (e.g. Roberts 1968; Busse 1970; Zhang 1992b; Jones *et al.* 2000; Dormy *et al.* 2004; Zhang & Liao 2004; Zhang *et al.* 2007), which involves determining the most unstable azimuthal wavenumber,  $m_c$ , at which convective instability occurs, and the corresponding critical value of the Rayleigh number,  $R = R_c$ , as a function of  $E$  and  $Pr$ . Subsequent work has considered the sequence of bifurcations that occur as  $R$  is increased (e.g. Zhang 1991, 1992a; Sun *et al.* 1993; Tilgner & Busse 1997; Grote & Busse 2001).

An important modification to the homogeneous problem in the geophysical context is the effect of inhomogeneities at the outer boundary (OB) of the spherical shell. This problem, called the *inhomogeneous problem* here, may also be applicable to other bodies such as extrasolar planets. As well as  $E$ ,  $R$  and  $Pr$ , the inhomogeneous problem is governed by a new nondimensional parameter,  $\epsilon$ , which describes the ratio of peak-to-peak thermal amplitude variations on the OB to the temperature difference between the boundaries. The azimuthal scale of the boundary variations, denoted by the wavenumber  $m_b$ , is also significant.

Zhang & Gubbins (1993), herein referred to as ZG93, investigated the inhomogeneous problem for low  $\epsilon$  and high  $E$ . In the Earth  $E$  is very small. Estimating  $\epsilon$  for the Earth

is problematic due to difficulties in estimating the superadiabatic heat flux; it is unlikely to be small, with mantle convection studies predicting anything from  $\epsilon = O(1)$  to  $\epsilon = \infty$  (Nakagawa & Tackley 2007). Furthermore, seismic tomography shows large scale anomalies at the base of the mantle (Masters *et al.* 1996) making  $m_b < m_c$  in the Earth. In this paper we extend the results of ZG93 by investigating the inhomogeneous problem at lower  $E$  and higher  $\epsilon$  for various scales of the boundary anomalies.

The inhomogeneous problem gives rise to two basic flows. One is convective, setting in as an instability of the basic state that is driven by a difference in temperature between the boundaries (Chandrasekhar 1961). This flow will be termed *buoyancy-driven* in this work. The other flow is a thermal wind maintained by the boundary variations, which will be called *boundary-driven*. While a stable equilibrium is possible for the convective flow alone (when  $R < R_c$ ), there is no such state for a finite value of  $\epsilon$  as the lateral variations drive a thermal wind (Zhang & Gubbins 1992). Thus no critical value of  $R$  exists for the inhomogeneous problem, where these two flows occur together.

The inhomogeneous problem was first studied in the infinite  $Pr$  limit by Zhang & Gubbins (1992), who simulated flows driven by the lateral variations. They observed a phase shift between the flow pattern and boundary anomalies due to a dominant thermal wind balance. ZG93 studied the effect of an inhomogeneous fixed temperature outer boundary condition on convective instability at infinite  $Pr$ , high  $E$  and low  $\epsilon$ . Using a boundary condition with  $m_b = m_c$ , which, following ZG93 we call *primary convection* to emphasise the wavenumber matching, they found stable (in the linear sense), steady solutions, where the homogeneous flow pattern attached, or ‘locked’, to the boundary anomalies. In this paper the term ‘steady’ describes a time-independent solution, while the term ‘locked’ is used to describe flows that attach to the boundary anomalies: locked solutions may be unsteady. In the neighbourhood of  $R_c$  ZG93 observed a resonance, with

kinetic energy reaching a peak at a value of  $R$ ,  $R_r$ , just above critical. Stable steady solutions bifurcated to time-dependent solutions at a value of  $R$  just above  $R_r$ , with the type of bifurcation dictated by the value of  $\epsilon$ . For low  $\epsilon$  the bifurcation is of Hopf type, leading to an oscillatory solution. For larger values of  $\epsilon$  the bifurcation is of saddle-node type, and sets in as a wave of infinite period. With  $m_b < m_c$ , called *secondary convection* here to emphasise the wavenumber mismatch, ZG93 obtained stable, steady solutions, albeit at higher values of  $\epsilon$ . The flow patterns were dominated by the scale of the boundary forcing but modulated by the scale of the most unstable mode. Unstable solutions exhibited wavenumber vacillations between the competing  $m_b$  and  $m_c$  modes.

In this work a large value of  $Pr$  is used that makes inertial forces negligible, an important ingredient for obtaining locked solutions (Zhang & Gubbins 1996). It has been found by experiment that  $Pr = 100$  gives a good approximation to the limit  $Pr \rightarrow \infty$  considered by ZG93 and this value is used throughout this paper. We demonstrate our findings using four values of the Ekman number,  $E = 8 \times 10^{-4}, 6 \times 10^{-4}, 3 \times 10^{-4}$ , and  $1.2 \times 10^{-4}$ . Supplementary calculations have been undertaken with  $E$  as low as  $2 \times 10^{-5}$ , however these larger values of  $E$  demonstrate new features more clearly. The free parameters are thus  $\epsilon$  and  $R$ . We keep  $R - R_c$  small to clearly demonstrate the effects of the inhomogeneous boundary condition.

Like ZG93 we employ fixed temperature boundary conditions in the problem formulation. The alternative prescription is fixed heat flux at the OB, the relevant boundary condition for the geophysical application. With homogeneous heat flux boundary conditions Gibbons *et al.* (2007) showed that  $m_c$  is not a simple function of  $E$  (see also Takehiro *et al.* (2002)), while fixed temperature boundary conditions yield a smooth monotonic dependence of  $m_c$  on  $E$ . In the moderately low  $E$  regime, which is the focus of this paper, the two boundary conditions yield very similar results (Gibbons *et al.*

2007). We therefore use fixed temperature boundary conditions to facilitate comparison with previous studies. We shall only consider equatorially symmetric boundary anomalies, where boundary temperature variations are mirrored in the equatorial plane, because the most unstable mode is always equatorially symmetric (Busse 1970) and both ZG93 and Gibbons & Gubbins (2000) found that equatorially antisymmetric boundary conditions have little effect on the solutions compared to the corresponding symmetric case. The inhomogeneous boundary condition used will be time-independent throughout.

The mathematical and numerical formulation are given in Section 2. The analysis is conducted in four stages: 1) Linear onset of convective instability is studied in Section 3 to determine  $R_c(E)$  and  $m_c(E)$ , which guide choices for the scale of the boundary inhomogeneities; 2) Steady, nonlinear, inhomogeneous solutions for various  $\epsilon$  in the neighbourhood of  $R_c$  using different scales of the boundary variations are found in Section 4; 3) Linear stability analysis of the steady solutions found in stage 2 is presented in Section 5; 4) Time-integration of the full nonlinear equations for solutions found to be linearly unstable are presented in Section 6. Conclusions are presented in Section 7.

## 2. Mathematical formulation

Consider a Boussinesq fluid of constant thermal diffusivity,  $\kappa$ , constant coefficient of thermal expansion,  $\alpha$ , and constant viscosity,  $\nu$ , confined to a rapidly rotating spherical shell of radial extent  $d = r_o - r_i$ . Here  $r_i$  corresponds to the inner boundary (IB) and  $r_o$  to the OB. Spherical polar coordinates,  $(r, \theta, \phi)$ , will be used throughout. The fluid rotates about the vertical  $\mathbf{z}$ -axis with angular velocity,  $\Omega$ . With no flow the basic temperature gradient,  $\nabla T_0 = -\beta \mathbf{r}$ , is produced by a uniform distribution of internal heat sources, where  $T_0$  is the basic state temperature and  $\beta$  is the temperature gradient of the internally heated basic state. Scaling length by the shell thickness,  $d$ , time by the thermal diffusion

time,  $d^2/\kappa$ , and  $\beta d^2$  as the unit of temperature, the nondimensional equations are

$$\frac{E}{Pr} \left( \frac{\partial \mathbf{u}}{\partial t} + (\mathbf{u} \cdot \nabla) \mathbf{u} \right) + \mathbf{z} \times \mathbf{u} = -\nabla P + Ra T \mathbf{r} + E \nabla^2 \mathbf{u}, \quad (2.1)$$

$$\frac{\partial T}{\partial t} + (\mathbf{u} \cdot \nabla) T = \nabla^2 T + 3, \quad (2.2)$$

$$\nabla \cdot \mathbf{u} = 0. \quad (2.3)$$

Here  $\mathbf{u}$  is the fluid velocity,  $P$  is the pressure, and  $T$  is the temperature. The aspect ratio,  $r_o/r_i$ , of the shell is set to 0.4 for comparison with ZG93. The Ekman number, Prandtl number, and modified Rayleigh number are

$$E = \frac{\nu}{2\Omega d^2}, \quad Pr = \frac{\nu}{\kappa}, \quad Ra = \frac{g\alpha\beta d^3}{2\Omega\kappa} = RE, \quad (2.4)$$

where  $g$  is the gravitational acceleration at the outer boundary. Gravity varies linearly with radius.

The velocity field is decomposed into toroidal and poloidal components

$$\mathbf{u} = \nabla \times (\mathcal{T}\mathbf{r}) + \nabla \times \nabla \times (\mathcal{P}\mathbf{r}). \quad (2.5)$$

Substituting (2.5) into (2.1) and applying  $\mathbf{r} \cdot \nabla \times$  and  $\mathbf{r} \cdot \nabla \times \nabla \times$  gives

$$E \left( \nabla^2 - \frac{1}{Pr} \frac{\partial}{\partial t} \right) L_2 \mathcal{T} = \frac{E}{Pr} \mathbf{r} \cdot \nabla \times [(\mathbf{u} \cdot \nabla) \mathbf{u}] - \mathbf{r} \cdot \nabla \times (\mathbf{z} \times \mathbf{u}), \quad (2.6)$$

$$E \left( \nabla^2 - \frac{1}{Pr} \frac{\partial}{\partial t} \right) L_2 \nabla^2 \mathcal{P} + Ra L_2 \mathcal{T} = -\frac{E}{Pr} \mathbf{r} \cdot \nabla \times \nabla \times [(\mathbf{u} \cdot \nabla) \mathbf{u}] - \mathbf{r} \cdot \nabla \times \nabla \times (\mathbf{z} \times \mathbf{u}), \quad (2.7)$$

where the operator  $L_2$  is defined as

$$L_2 = - \left[ \frac{1}{\sin \theta} \frac{\partial}{\partial \theta} \left( \sin \theta \frac{\partial}{\partial \theta} \right) + \frac{1}{\sin^2 \theta} \frac{\partial^2}{\partial \phi^2} \right]. \quad (2.8)$$

To compare with ZG93, impenetrable and stress-free boundary conditions are applied to

$\mathbf{u}$  at  $r_i$  and  $r_o$ , which become

$$\mathcal{P} = \frac{\partial^2 \mathcal{P}}{\partial r^2} = \left( \frac{\partial}{\partial r} - \frac{1}{r} \right) \mathcal{T} = 0, \quad (2.9)$$

upon using (2.5). We consider fixed temperature at the IB and OB, corresponding to

$$T(r_i) = 0, \quad T(r_o) = \epsilon f(r_o, \theta, \phi), \quad (2.10)$$

where  $f(r_o, \theta, \phi)$  defines the pattern of temperature variations on the OB,  $r = r_o$ . The spherical harmonic expansion of  $f(r_o, \theta, \phi)$  is normalised as

$$\int_0^{2\pi} \int_0^\pi f^2(r_o, \theta, \phi) \sin \theta d\theta d\phi = 1. \quad (2.11)$$

In this paper  $f$  is expressed by a single spherical harmonic, written  $Y_l^m$ . Only equatorially symmetric boundary variations are considered and so  $l = m$  in all the cases that follow. The parameter  $\epsilon$  in (2.10), the inhomogeneity parameter, is a measure of the amplitude of boundary variations and is defined as

$$\epsilon = \frac{T_B}{\beta d^2}, \quad (2.12)$$

where  $T_B$  is a measure of the peak-to-peak temperature variations on the boundary.

Equations (2.2), (2.6), and (2.7), together with the boundary conditions (2.9) and (2.10), form the inhomogeneous problem. The manifold of solutions is explored in four stages by the following sets of calculations.

### 2.1. Onset of convection with homogeneous boundary conditions

For the linear onset of convective instability with homogeneous boundaries ( $\epsilon = 0$ ) all nonlinear and inhomogeneous terms in (2.6) and (2.7) are neglected. An exponential time-dependence,  $\partial/\partial t = \sigma$ , is assumed, where  $\sigma = \sigma_r + i\sigma_i$  is the complex growth rate.

The equations thus become linear and form an eigenvalue problem for  $\sigma$ , which is solved by the implicitly restarted Arnoldi method (IRAM, Lehoucq *et al.* 1998). The largest real part of  $\sigma$  represents the rate of growth (decay) of the disturbance if  $\sigma_r > 0$  ( $< 0$ ). The imaginary part of  $\sigma$  determines whether the solution is steady ( $\sigma_i = 0$ ) or oscillatory ( $\sigma_i \neq 0$ ).

For each azimuthal wavenumber  $m$  and an initial guess for  $Ra$ , the eigensystem is solved for  $\sigma$ . An iterative method is used to determine the value of  $Ra$  that gives  $\sigma_r = 0$ . The most unstable mode,  $m_c$  is the mode having the lowest such  $Ra$ , which is the critical Rayleigh number  $Ra_c$ .

## 2.2. Locked, inhomogeneous solutions

To account for the inhomogeneous outer boundary, the temperature is decomposed as

$$T(r, \theta, \phi, t) = \Theta(r, \theta, \phi, t) + \epsilon f(r_o, \theta, \phi), \quad (2.13)$$

making the boundary conditions on the unknown temperature,  $\Theta$ , homogeneous. The nonlinear equations (2.6) and (2.7) become inhomogeneous,

$$E\nabla^2 L_2 \mathcal{T} = \frac{E}{Pr} \mathbf{r} \cdot \nabla \times [(\mathbf{u} \cdot \nabla) \mathbf{u}] - \mathbf{r} \cdot \nabla \times (\mathbf{z} \times \mathbf{u}), \quad (2.14)$$

$$E\nabla^2 L_2 \nabla^2 \mathcal{P} + Ra L_2 \Theta = -\epsilon Ra L_2 f - \frac{E}{Pr} \mathbf{r} \cdot \nabla \times \nabla \times [(\mathbf{u} \cdot \nabla) \mathbf{u}] - \mathbf{r} \cdot \nabla \times \nabla \times (\mathbf{z} \times \mathbf{u}), \quad (2.15)$$

$$\nabla^2 \Theta - (\mathbf{u} \cdot \nabla) \Theta + 3 = \epsilon (\mathbf{u} \cdot \nabla - \nabla^2) f. \quad (2.16)$$

It is anticipated that the wavenumber  $m_b$  will dominate the flow pattern in the neighbourhood of  $Ra_c$  (ZG93). We therefore neglect azimuthal wavenumbers that are not multiples of  $m_b$  in some numerical computations. This allows thousands of nonlinear calculations to be performed and enables the use of Floquet theory (Verhulst 1993) in

the instability analysis (section 2.3). Many computations have been performed with full resolution in azimuth to test the lower resolution calculations and results from these computations will be presented in the following sections. The assumption will be shown to be adequate for stable solutions.

The code used to compute locked, inhomogeneous solutions is documented in Gibbons *et al.* (2007) and reproduces the results of ZG93, who used a different code. The code does not timestep the equations; steady solutions are obtained by an iterative method.

### 2.3. Instability analysis

A perturbation analysis is used to explore the stability of the locked solutions computed in section 2.2. Let the locked solutions be denoted by  $(\mathcal{T}_0, \mathcal{P}_0, \Theta_0)$ , and general perturbations by  $\tilde{A}$ , where  $\tilde{A} \in \{\tilde{\mathcal{T}}, \tilde{\mathcal{P}}, \tilde{\Theta}\}$ . Substituting  $\mathcal{T} = \mathcal{T}_0 + \tilde{\mathcal{T}}$ ,  $\mathcal{P} = \mathcal{P}_0 + \tilde{\mathcal{P}}$ ,  $\Theta = \Theta_0 + \tilde{\Theta}$ , into equations (2.1) and (2.2) and neglecting products of the perturbations gives the following set of linear equations

$$E \left( \nabla^2 - \frac{\sigma}{Pr} \right) L_2 \tilde{\mathcal{T}} = \frac{E}{Pr} \mathbf{r} \cdot \nabla \times [(\mathbf{u}_0 \cdot \nabla) \tilde{\mathbf{u}} + (\tilde{\mathbf{u}} \cdot \nabla) \mathbf{u}_0] - \frac{E}{Pr} \mathbf{r} \cdot \nabla \times (\mathbf{z} \times \tilde{\mathbf{u}}), \quad (2.17)$$

$$E \left( \nabla^2 - \frac{\sigma}{Pr} \right) L_2 \nabla^2 \tilde{\mathcal{P}} + Ra L_2 \tilde{\Theta} = -\mathbf{r} \cdot \nabla \times \nabla \times [(\mathbf{u}_0 \cdot \nabla) \tilde{\mathbf{u}} + \quad (2.18)$$

$$(\tilde{\mathbf{u}} \cdot \nabla) \mathbf{u}_0] - \frac{E}{Pr} \mathbf{r} \cdot \nabla \times \nabla \times (\mathbf{z} \times \tilde{\mathbf{u}}),$$

$$(\nabla^2 - \sigma) \tilde{\Theta} - (\tilde{\mathbf{u}} \cdot \nabla) \Theta_0 - (\mathbf{u}_0 \cdot \nabla) \tilde{\Theta} + 3 = \epsilon (\tilde{\mathbf{u}} \cdot \nabla) f. \quad (2.19)$$

The system is linear and  $\mathbf{u}_0$ ,  $T_0$  are periodic in  $\phi$ , so Floquet theory may be applied to the  $\phi$ -dependence of the perturbations. We therefore define the perturbations,  $\tilde{A}$ , as

$$\tilde{A} = \sum_{l=1}^L \sum_{m=0}^l \tilde{A}_l^m(r) Y_l^m(\theta, \phi) \exp \{iM\phi + \sigma t\} \quad (2.20)$$

where  $\exp \{iM\phi\}$  is the Floquet factor, and the Floquet exponent,  $M$ , is an integer.

A specified value of  $M$  defines the subclasses of perturbations that are retained in the

solutions. When  $M = 0$  the azimuthal wavenumbers of the perturbation include

$$m = 0, m_c, 2m_c, 3m_c, \dots,$$

and for general  $M$ ,

$$m = 0, m_c - M, m_c + M, 2m_c - M, 2m_c + M, \dots,$$

and so on for  $M = 0, 1, \dots, m_c - 1$ . Often the complete set of  $M$ 's does not need to be computed as certain values of  $m_c$  can make different subclasses equivalent: for example, with  $m_c = 7$  subclasses defined by  $M = 1$  and  $M = 6$  are identical, as are  $M = 2$  and  $M = 5$ , and  $M = 3$  and  $M = 4$ .

The system (2.17)–(2.19) is an eigensystem for  $\sigma = \sigma_r + i\sigma_i$ , which is solved by IRAM. The most unstable mode is the mode with largest  $\sigma_r$ , which is found by testing all values of  $M$ . The code used for stability analysis is documented in Gibbons *et al.* (2007) and reproduces the results of ZG93.

#### 2.4. Time integration

To determine the properties of unstable solutions predicted by the linear analysis it is necessary to integrate the full set of nonlinear equations, (2.1)–(2.3), by timestepping. The details of the numerical method used here can be found in Willis *et al.* (2007); the code differs from that of Gibbons *et al.* (2007) and has been used as an independent verification of our results.

Initial conditions for the inhomogeneous solutions are taken from the corresponding homogeneous solutions. This allows us to track the initial response of the system to the imposed inhomogeneous boundary condition as well as its long-term evolution.

---

$E$	$m_c$	$Ra_c$	$\sigma_i$
$3.16 \times 10^{-3}$	6	17.1	-10.7
$8 \times 10^{-4}$	7	21.7	-45.0
$6 \times 10^{-4}$	8	22.6	-53.6
$3 \times 10^{-4}$	10	26.6	-90.8
$1.2 \times 10^{-4}$	14	34.7	-173.5

---

TABLE 1. Results of linear stability analysis for the onset of convection with homogeneous boundary conditions. For each value of  $E$  the most unstable mode,  $m_c$ , the corresponding critical modified Rayleigh number,  $Ra_c$ , and the drift rate,  $\sigma_i$ , are given. Negative values of  $\sigma_i$  indicate prograde drift. Data for the lowest value of  $E$  considered by ZG93,  $E = 3.16 \times 10^{-3}$ , are included for comparison.

### 3. Onset of convection with homogeneous boundary conditions

Results of linear stability analysis for the onset of convection with homogeneous boundaries are presented in table 1 for each value of  $E$  considered. The most unstable mode is always symmetric with respect to the equator and the value of  $m_c$  increases as  $E$  decreases. The radial length scale of the motions also decreases with  $E$ , however the axial length scale is large for all  $E$ : the flow is organised into rolls (see figure 3 below). The frequency is negative for every  $E$ , indicating prograde drift of the rolls. The travelling wave is steady in a frame of reference co-rotating with the rolls.

Table 2 shows the same information as table 1 but for  $Pr = \infty$ . Values of  $m_c$  and  $\sigma_i$  are identical to the case with  $Pr = 100$ . Values of  $Ra_c$  differ at the fourth significant figure between the two cases. It therefore appears that  $Pr = 100$  is a good approximation to the limit  $Pr \rightarrow \infty$  near the onset of convection. Calculations in the marginally supercritical regime undertaken with both  $Pr = 100$  and  $Pr = \infty$  further verify this.

### 4. Locked, inhomogeneous solutions

#### 4.1. Primary convection

Figure 1 shows kinetic energy as a function of  $Ra$  for  $E = 8 \times 10^{-4}$ ,  $6 \times 10^{-4}$ , and  $3 \times 10^{-4}$ . When  $E = 1.2 \times 10^{-4}$ , the lowest value of  $E$  reported here, there is no value of  $\epsilon$  that

---

E	$m_c$	$Ra_c$	$\sigma_i$
$3.16 \times 10^{-3}$	6	17.1	-10.7
$8 \times 10^{-4}$	7	21.7	-45.0
$6 \times 10^{-4}$	8	22.7	-53.6
$3 \times 10^{-4}$	10	26.7	-90.8
$1.2 \times 10^{-4}$	14	34.8	-173.7

---

TABLE 2. Same as table 1 but with  $Pr = \infty$ .

forces a steady solution for  $Ra \geq Ra_c$ . This interesting result will be discussed separately in section 6.

It is clear that no spatial resonance is observed in figure 1. The presence or otherwise of a resonance is a complicated issue that depends on both  $\epsilon$  and  $m_b$ . Figure 2 shows kinetic energy as a function of  $Ra$  for various  $E$  at three values of  $\epsilon$ . Solutions with  $E = 3.16 \times 10^{-3}$  and  $\epsilon = 0.18$  correspond to solutions obtained by ZG93. As  $E$  decreases with  $\epsilon = 0.18$ , the primary resonance observed by ZG93 disappears at  $E = 2.3 \times 10^{-3}$ . Increasing  $\epsilon$  to 0.3 results in an observed resonance when  $E = 2.5 \times 10^{-3}$ , however no other value of  $E$  considered shows resonance. When  $\epsilon$  is further increased to 0.5 resonance is not observed for any  $E$  considered. Hence large  $\epsilon$  and large  $m_b$  appear to destroy resonance, with no resonance observed for  $E < 2 \times 10^{-3}$ . At low  $E$ , resonance is prohibited because the boundary effects and the buoyancy-driven flow do not reinforce each other, as described below.

A stable solution is shown in figure 3 with its homogeneous counterpart. The homogeneous solution exhibits rolls aligned with the rotation axis and centred about the mid-radius of the shell [figures 3(d) and 3(f)]. The inhomogeneous solution, while also being nearly two-dimensional (figure 3(e)), contains two layers of rolls, one located near the IB and the other near the OB (figure 3(c)).

The two-layer flow pattern forms because, at low  $E$ , the radial length scale of the convection rolls is small, resulting in weak motion near the boundaries (figure 3(d)). Fluid

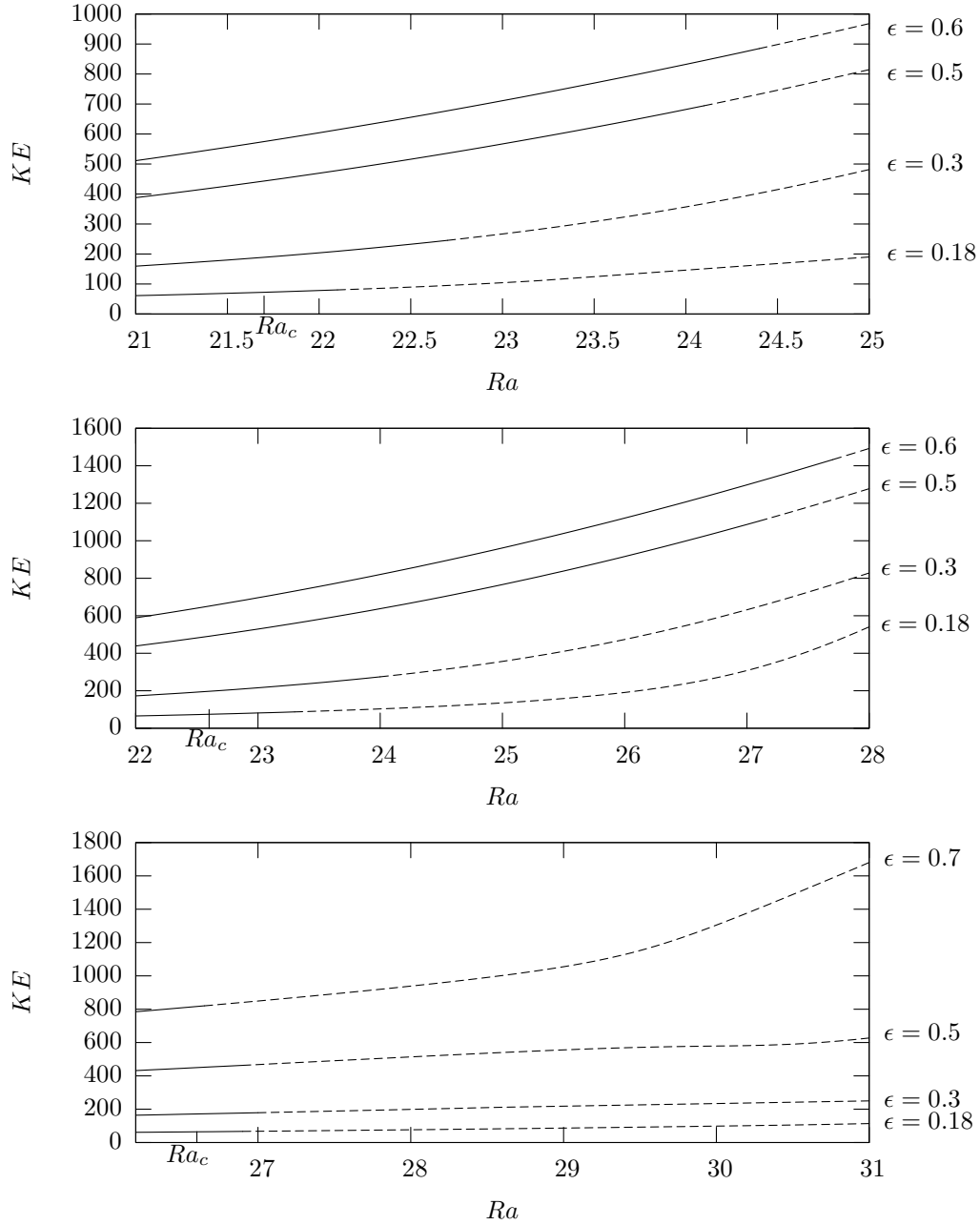


FIGURE 1. Kinetic energy as a function of  $Ra$  for selected values of  $\epsilon$ . Cases are  $E = 8 \times 10^{-4}$  with a  $Y_7^7$  boundary condition (top),  $E = 6 \times 10^{-4}$  with a  $Y_8^8$  boundary condition (middle), and  $E = 3 \times 10^{-4}$  with a  $Y_{10}^{10}$  boundary condition (bottom). Stable solutions are shown as thick lines, unstable solutions as broken lines. Lines are continued until the stability boundary is found. All stable solutions are steady. Solutions are obtained at intervals of  $Ra = 0.1$ .

near the IB is locked by the boundary anomalies acting near the poles of the outer spherical shell, forming the inner layer in figure 3(c). Near the OB boundary effects dominate,

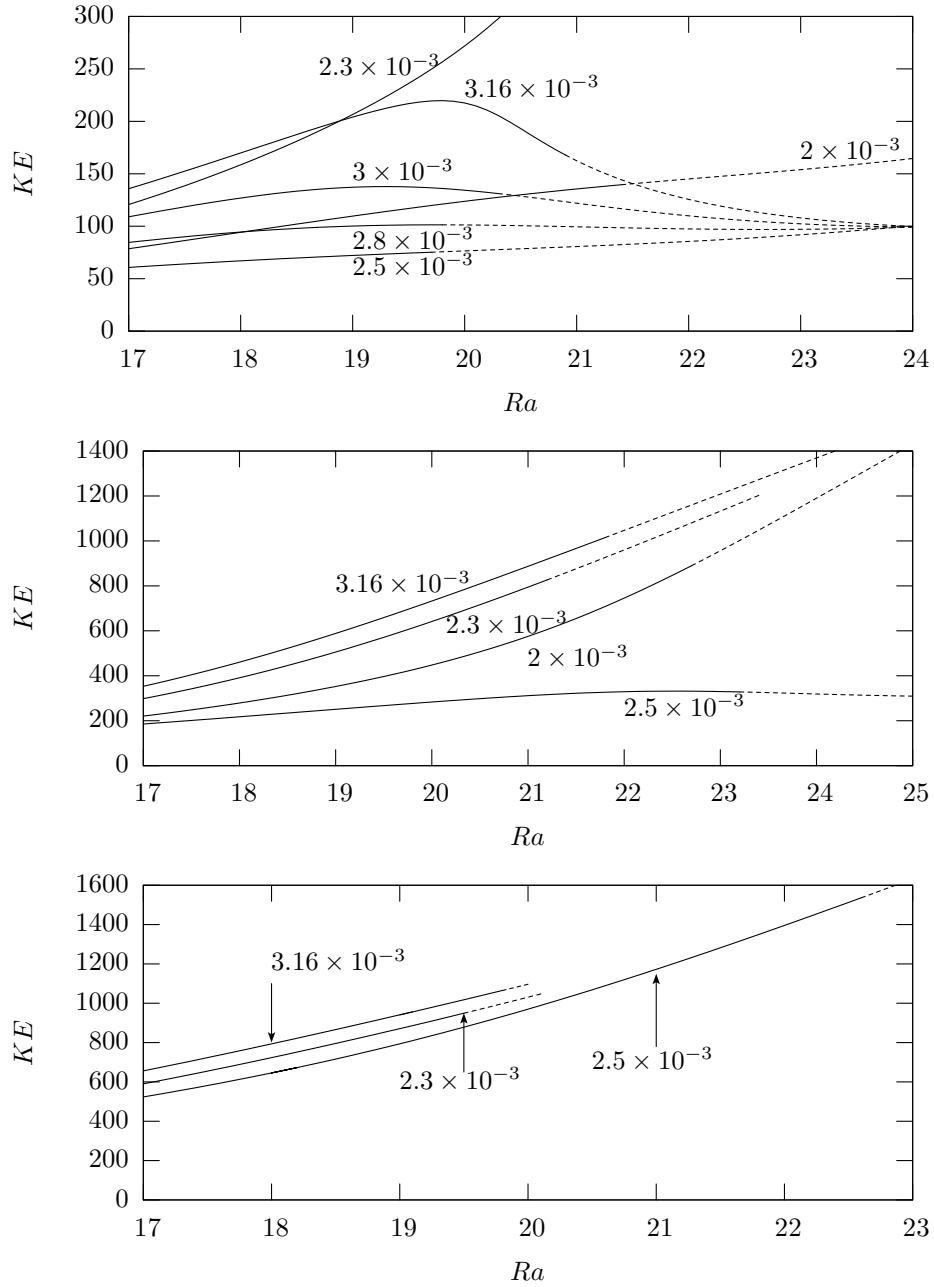


FIGURE 2. Kinetic energy as a function of  $Ra$  for various  $E$  with  $\epsilon = 0.18$  (top),  $\epsilon = 0.3$  (middle), and  $\epsilon = 0.5$  (bottom) with  $m_b = m_c$ . Stable solutions are shown as thick lines, unstable solutions as broken lines. Lines are continued until the stability boundary is found. All stable solutions are steady. Solutions are obtained at intervals of  $Ra = 0.1$ . The solution with  $E = 3.16 \times 10^{-3}$  and  $\epsilon = 0.18$  corresponds to a solution in figure 1 a) of ZG93; it is included for comparison with the earlier work.

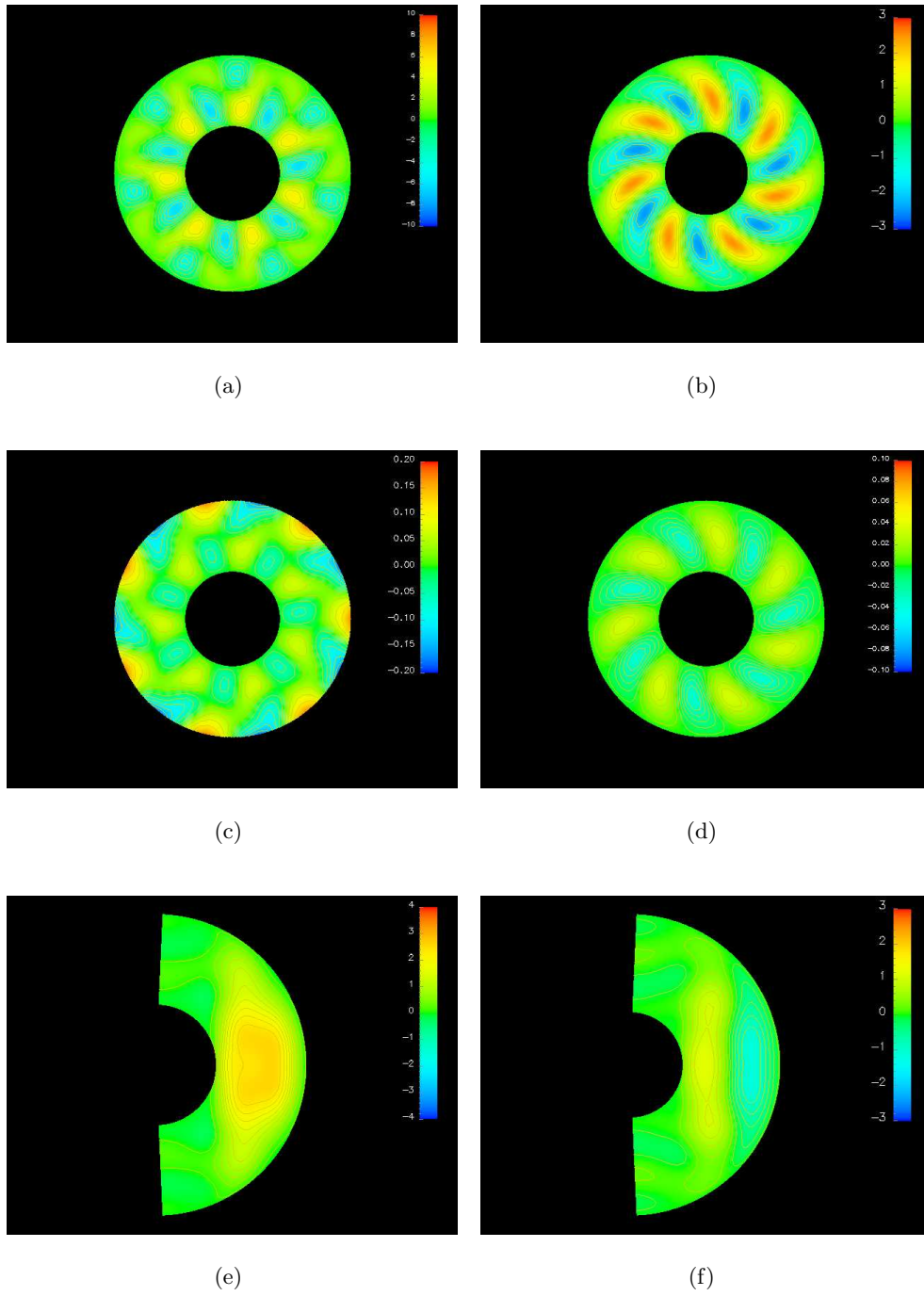


FIGURE 3. Properties of homogeneous (right) and inhomogeneous (left) solutions for  $Ra = 21.7$ ,  $E = 8 \times 10^{-4}$ ,  $\epsilon = 0.3$  with an imposed  $Y_7^7$  boundary condition: radial velocity ( $u_r$ ) in the equatorial plane (top row); temperature field in the equatorial plane (middle row);  $u_r$  in the meridional plane (bottom row), taken at  $\phi = \pi$ .  $\phi = 0$  is at the rightmost edge of the equatorial section. The homogeneous solution drifts in the prograde sense while the inhomogeneous solution is steady.

creating a second layer of rolls that are out of phase with the boundary temperature anomalies (figure 3(c)), as would result if convection was absent (Zhang & Gubbins 1992). Convection is suppressed near the mid-radius of the shell where it is preferred in the homogeneous case (compare figures 3(c) and 3(d)).

Figure 4 shows that the two-layer pattern persists at lower values of  $E$ , with both layers becoming more closely confined near the boundaries. As  $E$  decreases the interior flow is less affected by the boundary anomalies and hence larger values of  $\epsilon$  are required for locking (figure 1). However,  $\epsilon$  does not cause the two-layer pattern as it does not alter the imposed scale of the boundary anomalies.

This pattern does not arise at larger  $E$  because the radial length scale of the convection rolls is greater. The effects of the boundary anomalies penetrate deeper into the shell (compare figures 4(d), 4(c) and 3(a)) as large  $E$  gives low  $m_c (= m_b)$ . Hence there is no region of the shell in which convection or boundary effects dominate and the resulting interaction leads to steady solutions that retain the single-layer pattern seen in homogeneous convection, as found by ZG93. Calculations in figure 2 indicate that a transition from the single- to two-layer pattern occurs at  $E \approx 1.5 \times 10^{-3}$ , close to the value of  $E$  where  $m_c$  changes from  $m_c = 6$  to  $m_c = 7$ .

#### 4.2. *Secondary convection*

Figure 5 shows kinetic energy as a function of  $Ra$  for  $E = 6 \times 10^{-4}$ ,  $3 \times 10^{-4}$ , and  $1.2 \times 10^{-4}$ , when  $m_b = m_c/2$ . Larger values of  $\epsilon$  are required to obtain locked solutions than for the case  $m_b = m_c$  as found by ZG93. The spatial resonance phenomenon does not occur for any of the cases considered. We show that this may be explained by the dominance of the boundary-driven flows.

Locked solutions exist for  $E = 1.2 \times 10^{-4}$  when a  $Y_7^7$  boundary condition is imposed, indicating that boundary conditions with  $m_b < m_c$  are the most effective in obtaining

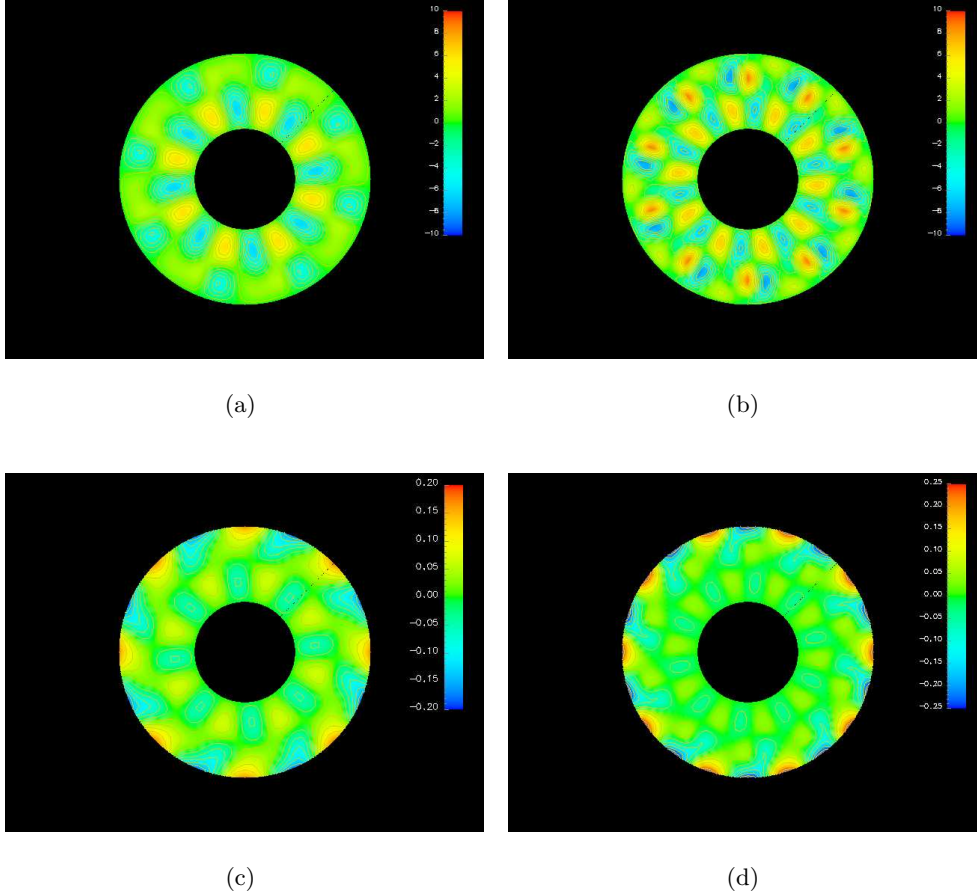


FIGURE 4.  $u_r$  in the equatorial plane (top) and  $T$  in the equatorial plane (bottom) for the inhomogeneous solutions with  $E = 6 \times 10^{-4}$ ,  $Ra = 22.6$  and  $\epsilon = 0.3$  with an imposed  $Y_8^8$  boundary condition (left), and  $E = 3 \times 10^{-4}$ ,  $Ra = 26.6$  and  $\epsilon = 0.5$  (right) with an imposed  $Y_{10}^{10}$  boundary condition. Meridional sections have been omitted as they are qualitatively identical to the case  $E = 8 \times 10^{-4}$  above. Both solutions are steady.

locked solutions as  $E$  decreases. At larger  $E$ , boundary conditions with  $m_b = m_c$  were found to be most effective (ZG93). The pattern of convection is shown in figure 6 for  $E = 1.2 \times 10^{-4}$ . The boundary mode dominates the convection pattern; it is modulated by the  $m_c = 14$  mode. High amplitude regions of  $u_r$  are out of phase with the boundary temperature anomalies because of the dominance of the inhomogeneous boundary condition. Figure 7 shows that the boundary mode dominates at higher  $E$ . With  $m_b = m_c/2$  the penetration depth of boundary anomalies is greater than for  $m_b = m_c$  and this can

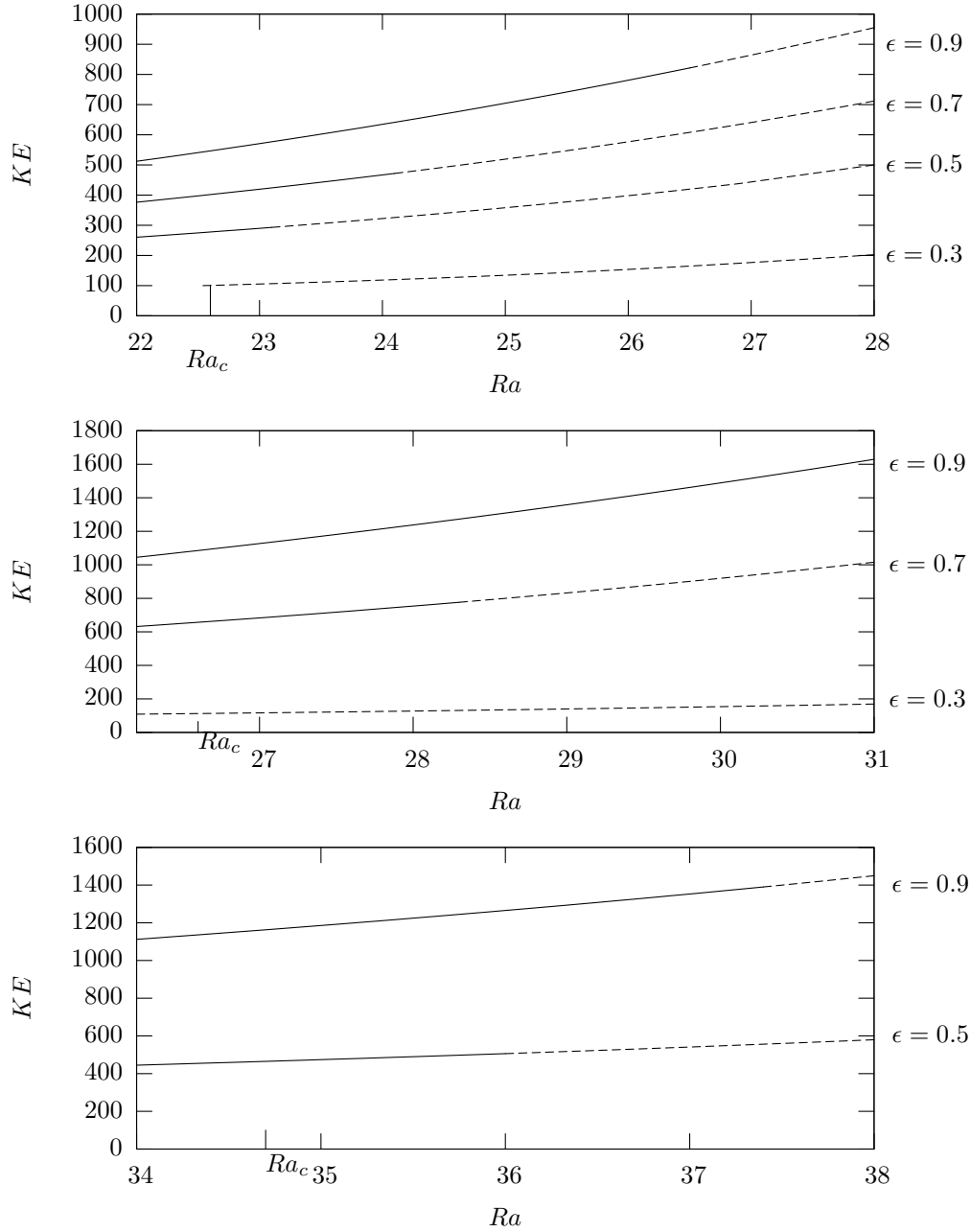


FIGURE 5. Kinetic energy as a function of  $Ra$  for selected values of  $\epsilon$ . Cases are  $E = 6 \times 10^{-4}$  ( $m_c = 8$ ) with an imposed  $Y_4^4$  boundary condition (top),  $E = 3 \times 10^{-4}$  ( $m_c = 10$ ) with an imposed  $Y_5^5$  boundary condition (middle), and  $E = 1.2 \times 10^{-4}$  ( $m_c = 14$ ) with an imposed  $Y_7^7$  boundary condition (bottom). Filled lines denote stable solutions; dashed lines denote unstable solutions. Curves are continued until the stability boundary has been determined. All stable solutions are steady. Solutions are obtained at intervals of  $Ra = 0.1$ .

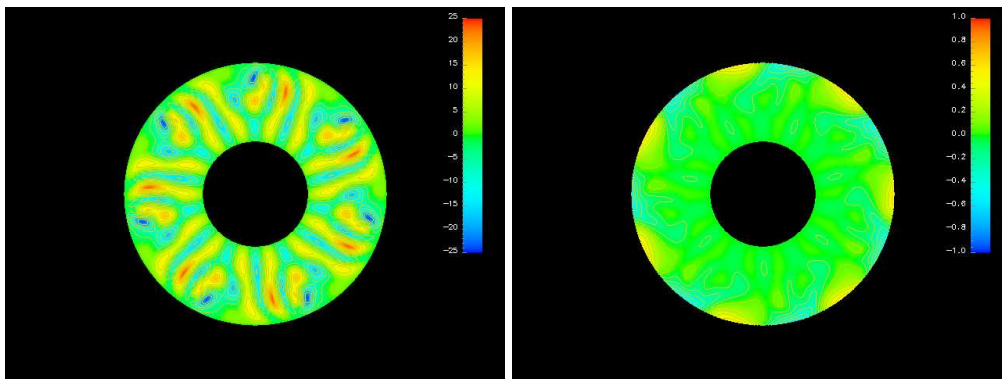


FIGURE 6.  $u_r$  (left) and  $T$  (right) in the equatorial plane for  $E = 1.2 \times 10^{-4}$ ,  $Ra = 34.7$  and  $\epsilon = 0.9$  with an imposed  $Y_7^7$  boundary condition. The solution is steady, equatorially symmetric, and dominated by the boundary mode,  $m_b = 7$ .

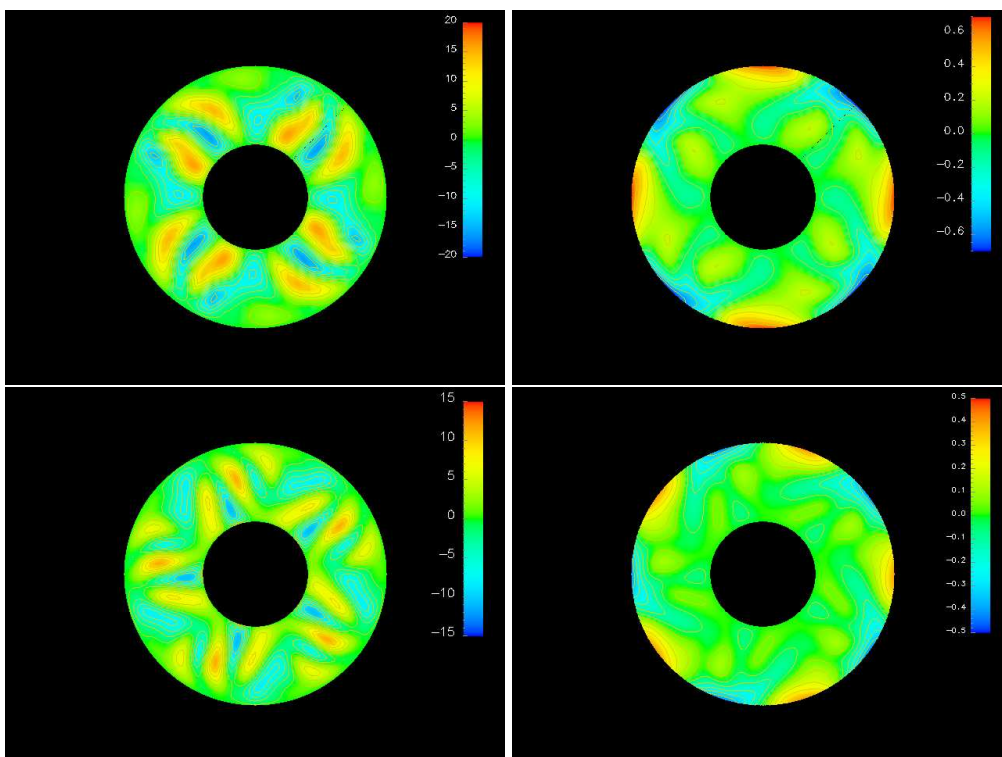


FIGURE 7.  $u_r$  (left) and  $T$  (right) in the equatorial plane for  $E = 6 \times 10^{-4}$ ,  $Ra = 22.6$ ,  $\epsilon = 0.9$  with an imposed  $Y_4^4$  boundary condition (top) and  $E = 3 \times 10^{-4}$ ,  $Ra = 26.6$ ,  $\epsilon = 0.9$  with an imposed  $Y_5^5$  boundary condition (bottom). Both solutions are steady and equatorially symmetric.

promote locking. Decreasing  $m_b$  further requires a larger  $\epsilon$  for locking because the amplitude of boundary effects weakens.  $\epsilon$  cannot be increased indefinitely as the steady state

becomes unstable to boundary-driven instabilities. Hence locked solutions are unlikely to exist for all values of  $m_b$ , especially when the difference between  $m_c$  and  $m_b$  is large.

## 5. Instability analysis

### 5.1. Stability of primary convection

Figure 8 displays instability curves for each value of  $E$  when  $m_b = m_c$ . Curves for  $E = 1.2 \times 10^{-4}$  are not shown as no steady solution exists from which to perturb. Solutions at higher values of  $\epsilon$  cannot be calculated as too much lateral heating induces an instability: no steady state exists to perturb. The drift rate,  $\sigma_i$ , is nonzero at all points on all curves, suggesting that the bifurcations are of Hopf-type, although the precise nature of any bifurcation cannot be determined with certainty without integrating the full nonlinear equations.

Solutions in figure 8 become unstable to perturbations from the  $M = 1$  and  $M = 2$  subclasses, in contrast to ZG93 who found most unstable modes with  $M = 0$ . The explanation is likely to lie with the resonance observed by ZG93 near  $Ra_c$ ; no resonance is observed here and instability sets in by a different mode breaking the constraint imposed by the boundary condition.

### 5.2. Stability of secondary convection

Figure 9 shows instability diagrams for  $E = 6 \times 10^{-4}$ ,  $3 \times 10^{-4}$ , and  $1.2 \times 10^{-4}$  when  $m_b = m_c/2$ . The stability boundaries for all  $E$  and  $\epsilon$  are characterised by  $\sigma_i \neq 0$ . Unstable solutions bifurcate from steady solutions with  $M = 0$  for all cases considered. This contrasts with the results of section 5.1 where  $M \neq 0$  is preferred. The change is due to the introduction of a new, competing scale. With  $m_b \neq m_c$  the interaction between the two dominant modes results in the loss of stability of locked solutions.

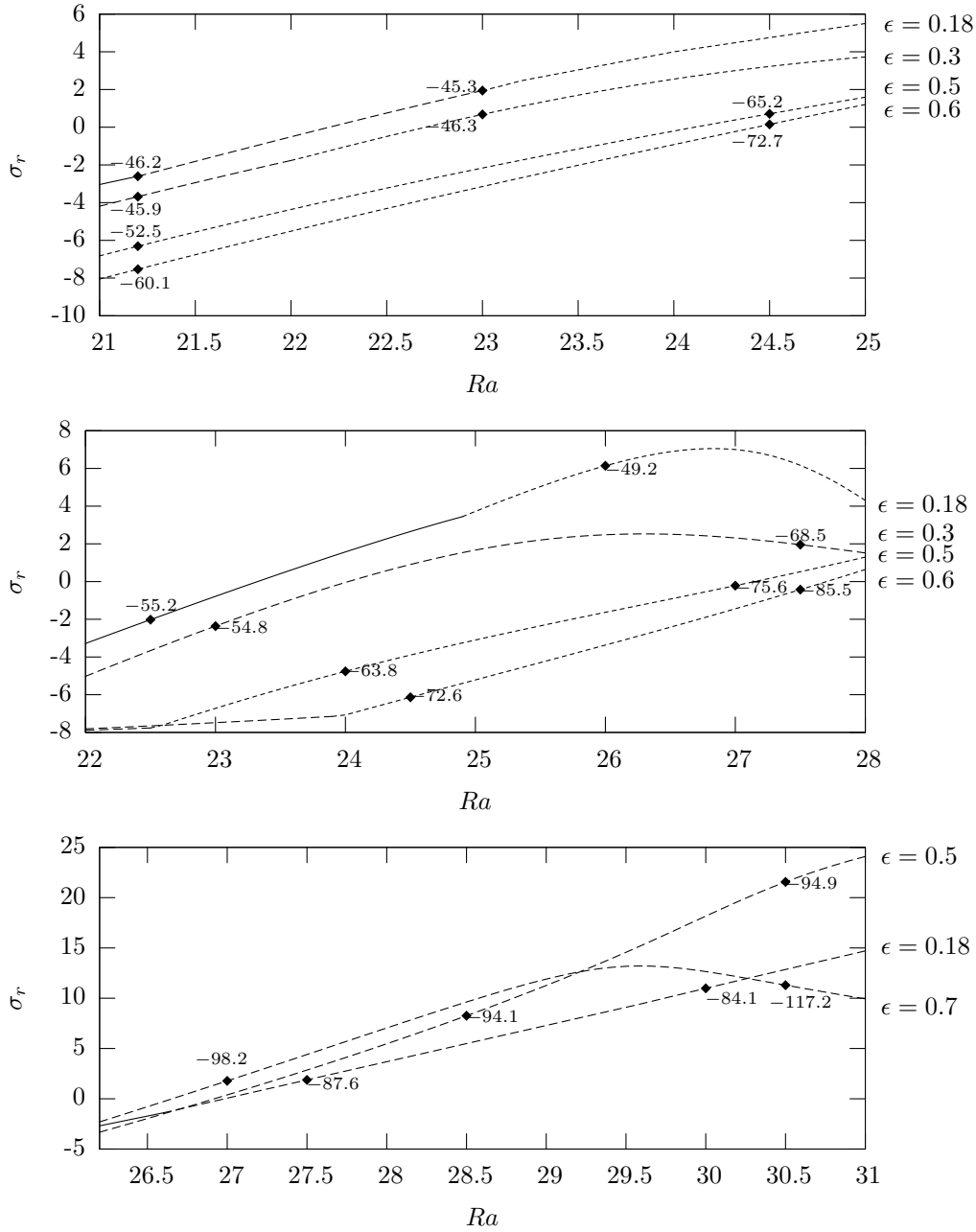


FIGURE 8.  $\sigma_r$  as a function of  $Ra$  for (top to bottom)  $E = 8 \times 10^{-4}$ ,  $6 \times 10^{-4}$ , and  $3 \times 10^{-4}$  with  $m_b = m_c$ . Different curves represent different values of  $\epsilon$ . Numbers next to the curves denote the frequency,  $\sigma_i$ , of the most unstable disturbance at that point on the curve. Full lines show that the most unstable disturbance is from the  $M = 0$  subclass; long dashed lines show the  $M = 1$  subclass; short dashed lines show the  $M = 2$  subclass (see section 2.3 for details).

## 6. Time integration

### 6.1. Unstable primary solutions

Figure 10 shows a comparison between two nonlinear solutions at, and just above, the stability boundary where the linear analysis predicts  $M = 2$  as the most unstable per-

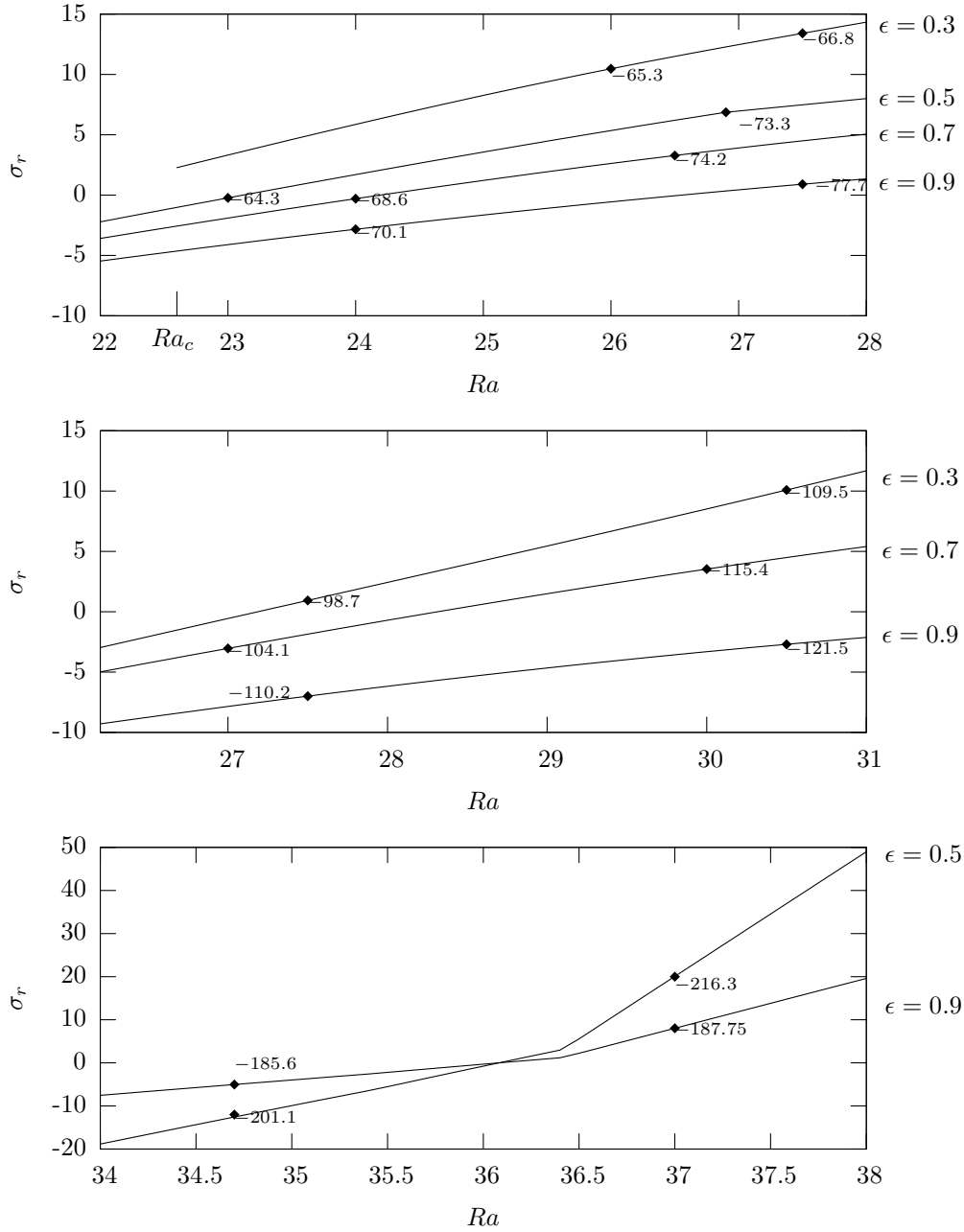


FIGURE 9. Stability curves for (top to bottom)  $E = 6 \times 10^{-4}$ ,  $3 \times 10^{-4}$ , and  $1.2 \times 10^{-4}$  with  $m_b = m_c/2$ . Different curves represent different values of  $\epsilon$ . Numbers next to the curves denote the frequency,  $\sigma_i$ , of the most unstable mode at that point on the curve. Filled lines show that the most unstable disturbance is from the  $M = 0$  subclass.

turbation subclass. Both solutions are periodic in time with prograde drift near the mid-radius of the shell, but they differ markedly in planform. At the stability boundary modes from the  $M = 2$  subclass are barely visible; the equatorial pattern is dominated by

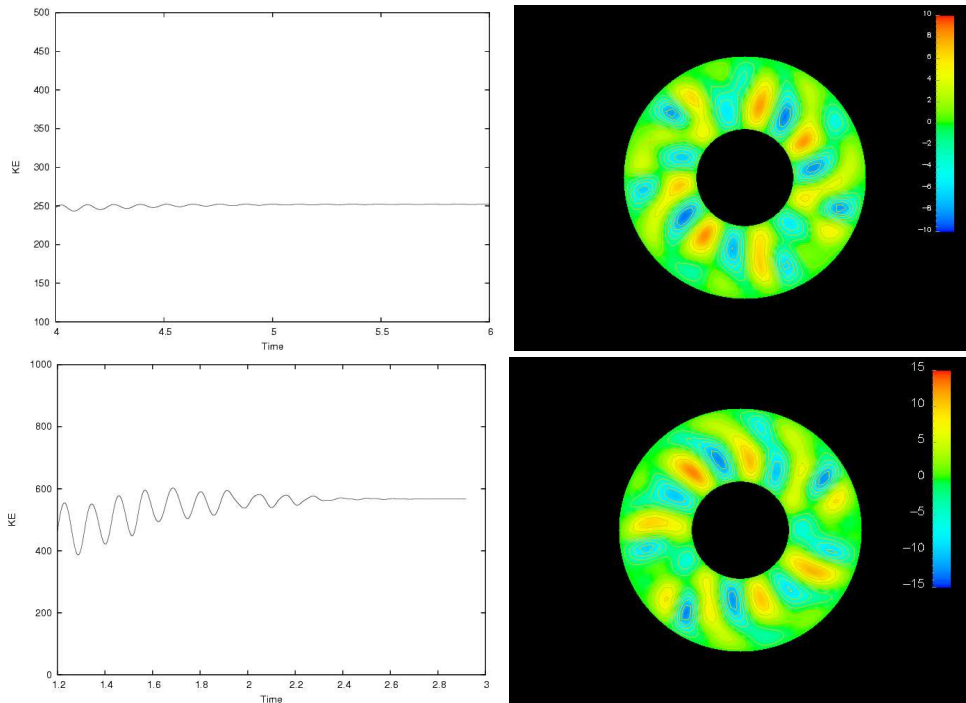


FIGURE 10. Kinetic energy time-series (left) and snapshots of  $u_r$  in the equatorial plane (right) for  $E = 8 \times 10^{-4}$ ,  $\epsilon = 0.3$  and  $m_b = m_c = 7$ , with  $Ra = 23$  (top) and  $Ra = 25$  (bottom). The former case is at the stability boundary, while the latter is above the stability boundary. Both solutions are periodic, drifting in the prograde sense, and symmetric with respect to the equatorial plane.

7 pairs of convection cells, unevenly organised in azimuth. Above the stability boundary the pattern is dominated by the  $m = 9$  mode (a member of the  $M = 2$  subclass) and modulated by a large  $m = 7$  mode. Stationary flows near the boundaries are observed as in previous sections. Steady solutions that become unstable to perturbations from the  $M = 1$  subclass (e.g. for  $E = 3 \times 10^{-4}$  in figure 8) display similar properties. Clearly the effect of the imposed boundary condition diminishes quickly once  $Ra$  is increased past the stability boundary for locked solutions.

### 6.2. Unstable secondary solutions

Figure 11 shows a periodic solution of secondary convection at the stability boundary where linear analysis predicts  $M = 0$  as the most unstable perturbation subclass. The equatorial flow pattern contains four persistent centres at  $\phi = \pi/4, 3\pi/4, 5\pi/4$ , and

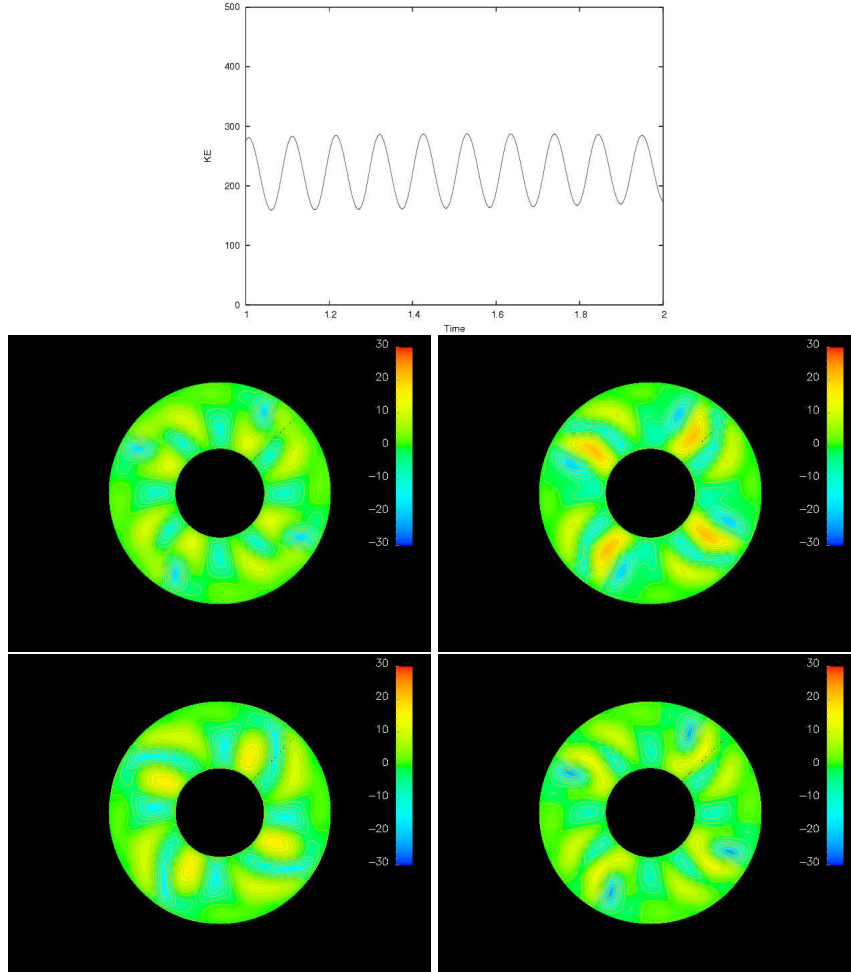


FIGURE 11. Kinetic energy time series (top) and snapshots of  $u_r$  in the equatorial plane for  $Ra = 24.1$ ,  $E = 6 \times 10^{-4}$ ,  $\epsilon = 0.7$  with  $m_b = 4$ . Snapshots are evenly spaced in time, spanning one period of the oscillation, and should be left-right and top-bottom. The solution is equatorially symmetric, so meridional sections have been omitted.

$7\pi/4$  where convection rolls become trapped, forming a nest. Rolls drift between the nests. Rolls confined within the nests are time-dependent but do not break out of the nests. Nests are out of phase with the boundary anomalies, illustrating the dominance of the boundary effects. Another example of this type of flow pattern is shown in figure 12, which is above the stability boundary, showing that this behaviour persists to higher values of  $Ra$ .

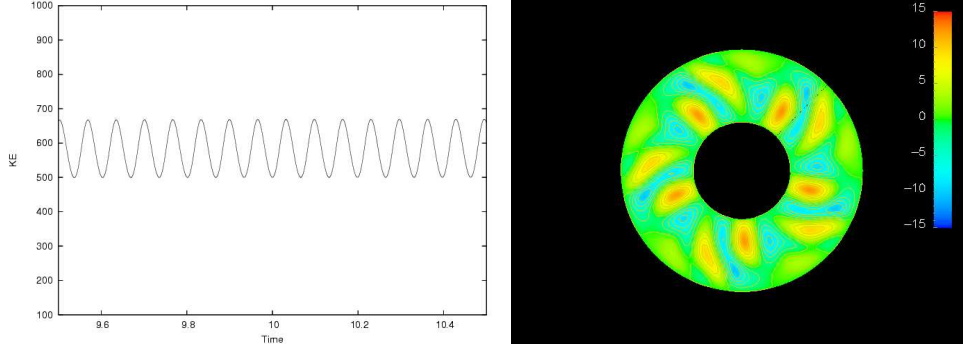


FIGURE 12. Kinetic energy time series (left) and a snapshot of  $u_r$  in the equatorial plane (right) for  $E = 3 \times 10^{-4}$ ,  $Ra = 28.5$ ,  $\epsilon = 0.7$  with  $m_b = 5$ . Linear analysis predicts  $M = 0$  as the most unstable perturbation subclass. The solution is periodic, equatorially symmetric, and contains five persistent nests of convection rolls.

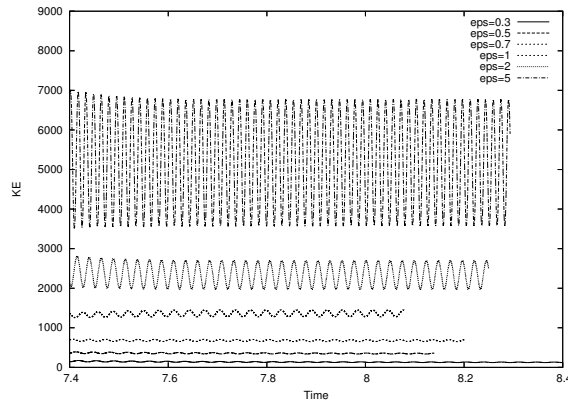


FIGURE 13. Kinetic energy time series for selected values of  $\epsilon$  at  $E = 1.2 \times 10^{-4}$  and  $Ra = 34.7$  with  $m_b = m_c = 14$ . All solutions are periodic.

### 6.3. Solutions for $E \leq 1.2 \times 10^{-4}$

#### 6.3.1. Primary convection

No values of  $\epsilon$  in the range  $0.1 \leq \epsilon \leq 10$  force a steady solution for  $E < 1.5 \times 10^{-4}$  when  $Ra \geq Ra_c$ . Kinetic energy time series for selected values of  $\epsilon$  are shown in figure 13. Low  $\epsilon$  solutions are dominated by the buoyancy-driven flow and slightly modulated by boundary effects. Solutions with  $\epsilon \geq 5$  are unstable because of large temperature variations on the boundary.

A periodic solution for  $\epsilon = 0.7$  is shown in figure 14 at evenly-spaced time points spanning one period of oscillation in figure 13. The pattern maintains a striking three-layer

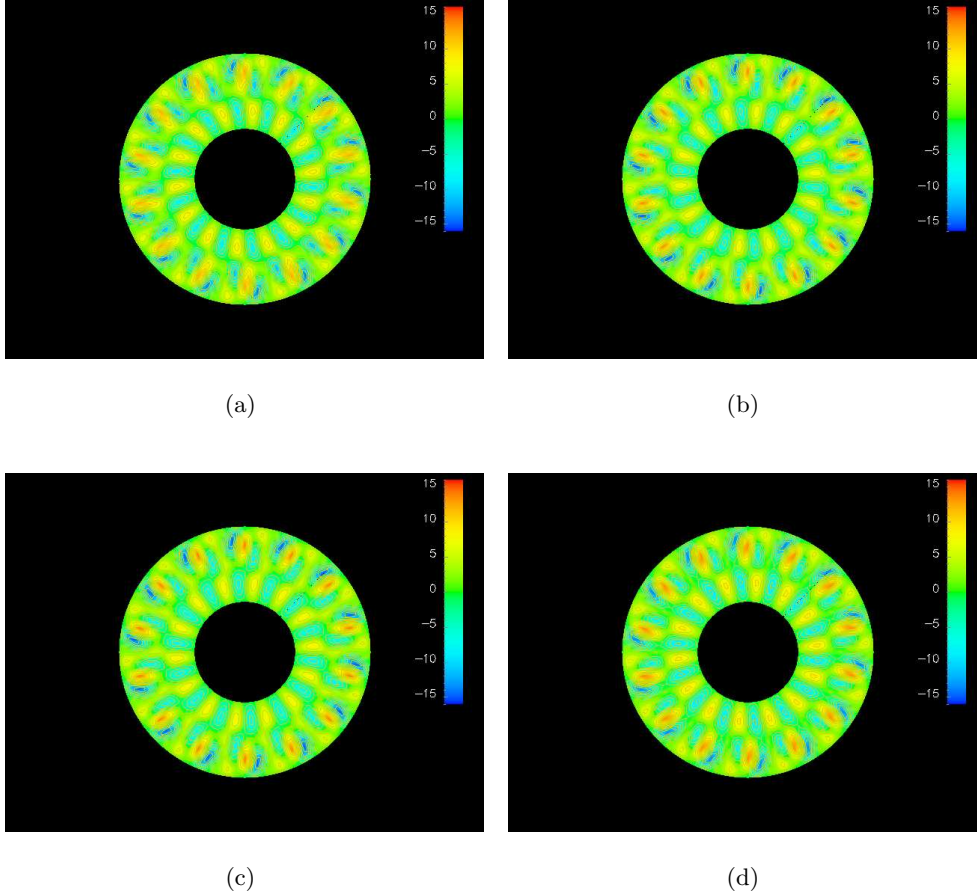


FIGURE 14. Snapshots of  $u_r$  in the equatorial plane, at equally-spaced time points spanning one period, for  $E = 1.2 \times 10^{-4}$ ,  $Ra = 34.7$ ,  $\epsilon = 0.7$  with an imposed  $Y_{14}^{14}$  boundary condition, showing the oscillation in the interior of the domain. Snapshots should be viewed in alphabetical order.

structure with stationary layers near the boundaries and drift confined to a relatively thin region between these layers. The middle layer is where convection rolls establish in the homogeneous problem. Because of the small radial length scales of the buoyancy-driven and boundary-driven flows, the boundary anomalies are unable to overcome the convective driving, even at the stability boundary of homogeneous convection, and therefore no stable equilibrium exists. Figure 15 shows that such a flow occurs at  $E = 2 \times 10^{-5}$ .

Increasing  $\epsilon$  increases the amplitude of the boundary-driven flow, but the radial scale of this flow is determined by  $m_b$ . Hence a larger  $\epsilon$  has little effect on the middle layer and

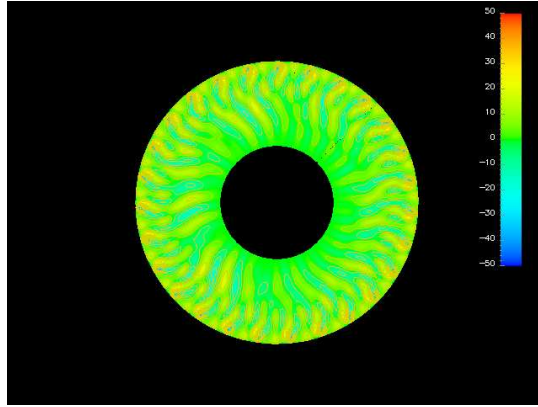


FIGURE 15. Snapshot of  $u_r$  in the equatorial plane for  $E = 2 \times 10^{-5}$ ,  $Ra = 62$ ,  $\epsilon = 1$ , with an imposed  $Y_{27}^{27}$  boundary condition. The most unstable mode  $m_c = 27$ , and  $Ra_c = 61.1$ . The solution is equatorially symmetric.

an  $\epsilon \geq 5$  produces vigorous motions due to the large boundary temperature variations.

Locking can only be achieved with  $m_b < m_c$  (section 4.2).

ZG93 considered an analogous Landau equation as a framework for understanding locked solutions. The framework equation implies that there always exists an  $\epsilon$  that will yield a steady solution for any amplitude of the driving force. The result in this section shows the shortcomings of this analogue. The framework equation does not account for the Coriolis force, yet it is the rotation that dictates the selection of the mode at the onset of convective instability. The dominant scales of the convective flow and the boundary anomalies, together with  $\epsilon$ , determine whether a locked solution is obtained.

### 6.3.2. Secondary convection

No locked solutions have been found at  $E = 1.2 \times 10^{-4}$  for  $m_b < 7$ . Figure 16 shows a comparison of unstable nonlinear solutions with different applied boundary inhomogeneities. The kinetic energy time series for  $m_b = 2$  is highly time-dependent, while for  $m_b = 4$  the solution is periodic. This demonstrates the weakening of boundary effects as  $m_c - m_b$  grows. Both solutions display the nesting of convection rolls shown in section 6.2, with the number of nests dictated by the imposed scale of the boundary condition.

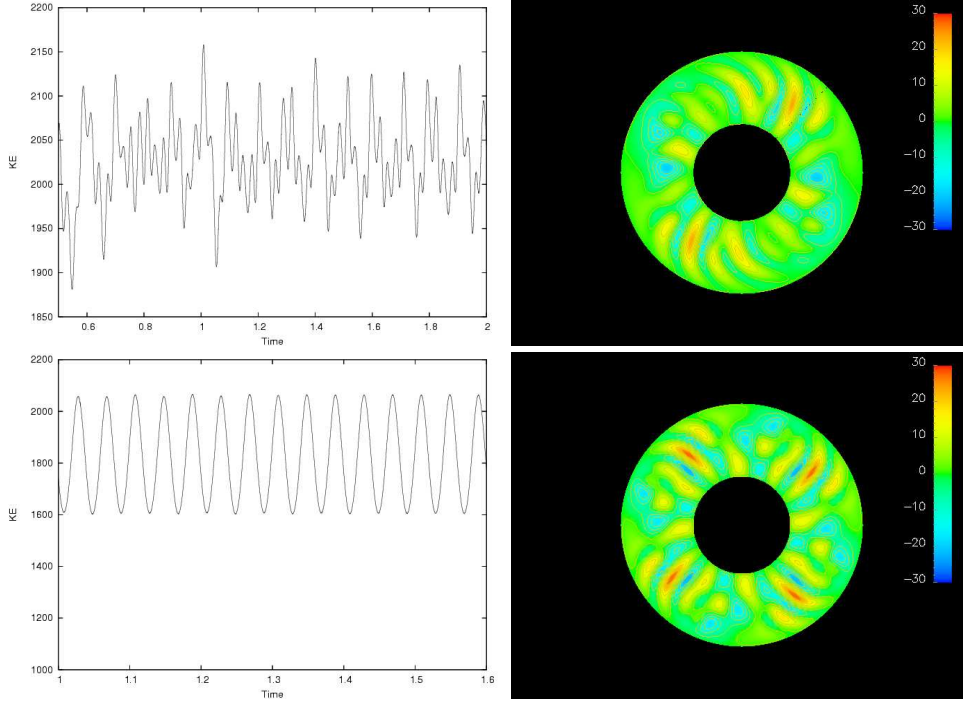


FIGURE 16. Kinetic energy time series (left) and snapshots of  $u_r$  in the equatorial plane (right) for  $E = 1.2 \times 10^{-4}$ ,  $Ra = 34.7$ ,  $\epsilon = 0.9$  with  $m_b = 2$  (top) and  $m_b = 4$  (bottom). The solutions are equatorially symmetric so meridional sections have been omitted.

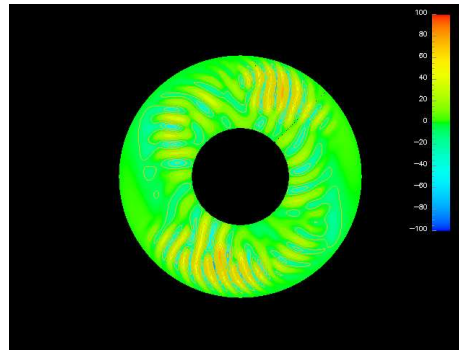


FIGURE 17. Snapshot of  $u_r$  in the equatorial plane for  $E = 2 \times 10^{-5}$ ,  $\epsilon = 1$ , and  $Ra = 62$  using a boundary condition with  $m_b = 2$ . The most unstable mode is  $m_c = 27$  and  $Ra_c = 61.1$ . The solution is equatorially symmetric.

Nesting becomes more prominent when the wavenumbers  $m_c$  and  $m_b$  differ substantially: the effect is much weaker for the solutions of section 6.2. Further calculations have shown that such solutions persist to  $E = 2 \times 10^{-5}$ , shown in figure 17, and up to a value of  $Ra$  that is twice supercritical.

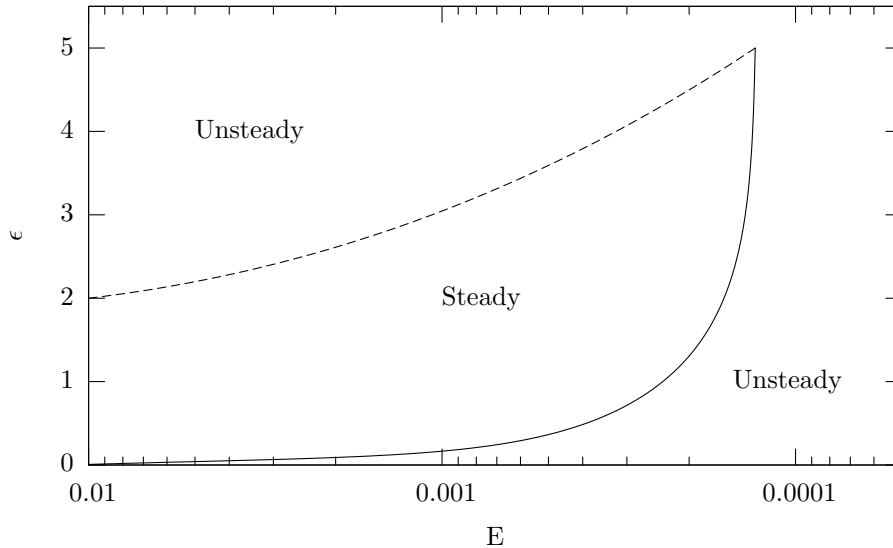


FIGURE 18. Schematic diagram of the boundaries between steady and unsteady solutions in the  $(E, \epsilon)$  plane for inhomogeneous convection at  $Ra = Ra_c$  with  $m_b = m_c$ . The solid line describes the minimum value of  $\epsilon$  for a given  $E$  that produces a steady, locked solution. Above the dashed line large lateral temperature variations on the OB prevent locking.

## 7. Conclusion

Our principal conclusion is that boundary conditions having spatial variations larger than the preferred mode of homogeneous convection ( $m_b < m_c$ ) are most effective in obtaining steady solutions as  $E$  decreases. When  $m_b = m_c$ , steady solutions occur, shown schematically in figure 18 for  $Ra = Ra_c$ . The minimum value of  $\epsilon$  needed to obtain a locked solution increases rapidly as  $E$  becomes small (solid line). Large values of  $\epsilon$  destabilise the system due to lateral heating (dashed line) and the two curves therefore intersect. Such a region was not found for boundary conditions with  $m_b < m_c$ . This may be due to the larger radial lengthscale of boundary conditions with  $m_b < m_c$  than those with  $m_b = m_c$ : in the former case fluid motions are suppressed deeper into the shell, with boundary effects dominating if  $\epsilon$  is high enough.

The spatial resonance phenomenon observed by ZG93 disappears when  $E$  is decreased or  $\epsilon$  is increased. This potentially important result does not have a simple explanation, partly because resonance is a nonlinear phenomenon: it is related to the amplitude of

convection, which for a given  $E$  is dictated primarily by  $\epsilon$  in the neighbourhood of  $Ra_c$ . We suggest that loss of resonance at low  $E$  occurs because of the small characteristic scales of the buoyancy-driven flow and the boundary anomalies: the boundary anomalies no longer reinforce the buoyancy-driven flow and a two-layer flow pattern emerges. Changing  $\epsilon$  does not affect the characteristic scales of the flow and boundary anomalies; we may expect an absence of resonance at low  $E$  for any  $\epsilon > 0$ , however for large  $E$  a different mechanism must occur to produce the behaviour in figure 2. It is the nonlinear interactions between the boundary anomalies and the buoyancy-driven flow that ultimately determine whether a resonance exists at high  $\epsilon$  and it is this complexity that prevents a more detailed understanding of the resonance phenomenon.

Solutions of secondary convection ( $m_b < m_c$ ) are summarised in figure 19 for two cases: 1) when  $m_b = m_c/2$ , the case studied in detail in this paper; 2) when  $m_b = 2$ , the geophysically relevant case. When  $m_b = m_c/2$  steady solutions are always possible for the range of  $E$  studied. For  $E \leq 6 \times 10^{-4}$ , solutions in the neighbourhood of  $Ra_c$  show that convection rolls cluster into nests that are out of phase with the boundary anomalies and remain trapped for many thermal diffusion times. Our calculations indicate that nested solutions appear abruptly as  $E$  is decreased and are insensitive to the value of  $\epsilon$  (shown by a dashed line in figure 19). When  $m_b = 2$  solutions are always unstable for the range of  $E$  considered. Our calculations indicate that nesting is weakly dependent on  $\epsilon$  for this case: if  $\epsilon$  is too small nesting is not observed; however nesting appears to occur for a wide range of  $\epsilon$ .

Nested solutions may be relevant to the Earth where the magnetic field in the historical record shows four concentrations of intense flux (Jackson *et al.* 2000), which could be maintained by persistent large-scale fluid downwellings (Willis *et al.* 2007). At low  $E$  this is unlikely to occur due to the small scales, which are dynamically preferred, but may be

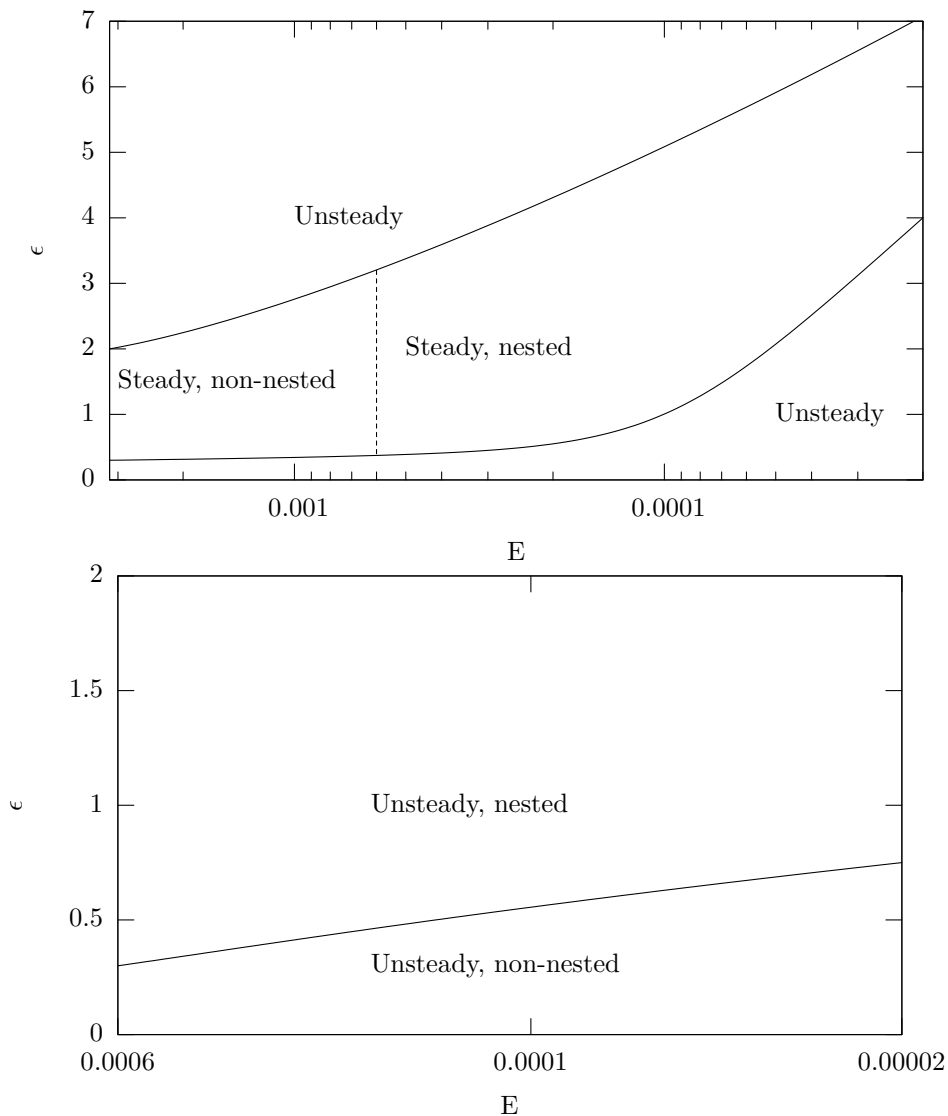


FIGURE 19. Schematic diagram of the boundaries between steady and unsteady solutions in the  $(E, \epsilon)$  plane for inhomogeneous convection for  $Ra$  in the neighbourhood of  $Ra_c$  with  $m_b = m_c/2$  (top) and  $m_b = 2$  (bottom).

produced by the nests of convection cells found in this paper. Nesting can produce large scale features and it is possible that the Earth contains two such nests due to a dominant mantle anomaly with  $m_b = 2$ .

It is interesting to consider the effect of an imposed inhomogeneous heat flux at the OB rather than the imposed fixed temperature considered in this paper. Heat flux boundary conditions tend to favour longer length scales than temperature boundary conditions near

the onset of convection (Glatzmaier & Gilman 1981; Takehiro *et al.* 1999, e.g.); however the discrepancy disappears at high rotation rates (Gibbons *et al.* 2007). It can therefore be anticipated that nested solutions exist with fixed heat flux at the outer boundary as long as  $m_b$  is sufficiently lower than the  $m_c$ , as we argue for the case of fixed temperature boundaries.

This work was supported by NERC Consortium Grant *Deep Earth Systems O/2001/00668*.

C. Davies is supported by a NERC E-science research studentship. The authors would like to thank Professor C. Jones and Dr B. Sreenivasan for helpful discussions. The comments of three anonymous reviewers helped to improve the original manuscript.

#### REFERENCES

- BUSSE, F.H. 1970 Thermal instabilities in rapidly rotating systems. *J. Fluid Mech.* **44**, 441–460.
- CHANDRASEKHAR, S. 1961 *Hydrodynamic and Hydromagnetic Stability*. Dover.
- DORMY, E., SOWARD, S., JONES, C.A., JAULT, D. & CARDIN, P. 2004 The onset of thermal convection in rotating spherical shells. *J. Fluid Mech.* **501**, 43–70.
- GIBBONS, S.J. & GUBBINS, D. 2000 Convection in the Earth’s core driven by lateral variations in core-mantle boundary heat flux. *Geophys. J. Int.* **142**, 631–642.
- GIBBONS, S.J., GUBBINS, D. & ZHANG, K 2007 Convection in a rotating spherical shell with inhomogeneous heat flux at the outer boundary. *Geophys. Astrophys. Fluid Dyn.* **101**, 347–370.
- GLATZMAIER, G.A. & GILMAN, P.A. 1981 Compressible convection in a rotating spherical shell. IV . Effects of viscosity, conductivity, boundary conditions, and zone depth. *Astrophysical Journal Supplement Series* **47**, 103–115.
- GROTE, E. & BUSSE, F.H. 2001 Dynamics of convection and dynamos in rotating spherical fluid shells. *Fluid Dyn. Res.* **28**, 349–368.
- JACKSON, A., JONKER, A.R.T. & WALKER, M.R. 2000 Four centuries of geomagnetic secular variation from historical records. *Phil. Trans. R. Soc. Lond. A* **358**, 957–990.

- JONES, C.A., SOWARD, A.M. & MUSSA, A.I. 2000 The onset of thermal convection in a rapidly rotating sphere. *J. Fluid Mech.* **405**, 157–179.
- LEHOUCQ, R.B., SORENSEN, D.C. & YANG, C. 1998 ARPACK users guide: solution of large scale eigenvalue problems by the implicitly restarted Arnoldi method. *Philadelphia, PA:SIAM*, <http://www.caam.rice.edu/software/ARPACK/UG/ug.htm> .
- MASTERS, G., JOHNSON, S., LASKE, G. & BOLTON, H.F. 1996 A shear-velocity model of the mantle. *Phil. Trans. R. Soc. Lond. A* **354**, 1385–1411.
- NAKAGAWA, T. & TACKLEY, P.J. 2007 Lateral variations in CMB heat flux and deep mantle seismic velocity caused by a thermal-chemical-phase boundary layer in 3D spherical convection. *Earth Planet. Sci. Lett.* **271**, 348–358.
- ROBERTS, P.H. 1968 On the thermal instability of a rotating-fluid sphere containing heat sources. *Phil. Trans. R. Soc. Lond. A* **263**, 93–117.
- SUN, Z-P., SCHUBERT, G. & GLATZMAIER, G.A. 1993 Transitions to chaotic thermal convection in a rapidly rotating spherical fluid shell. *Geophys. Astrophys. Fluid Dyn.* **69**, 95–131.
- TAKEHIRO, S., ISHIWATARI, M., NAKAJIMA, K. & HAYASHI, Y. 1999 The effects of thermal boundary conditions on convection in rapidly rotating spherical shells. *Theoret. Appl. Mech.* **48**, 415–421.
- TAKEHIRO, S., ISHIWATARI, M., NAKAJIMA, K. & HAYASHI, Y. 2002 Linear stability of thermal convection in rotating systems with fixed heat flux boundaries. *Geophys. Astrophys. Fluid Dyn.* **96**, 439–459.
- TILGNER, A. & BUSSE, F.H. 1997 Finite-amplitude convection in rotating spherical fluid shells. *J. Fluid Mech.* **332**, 359–376.
- VERHULST, F. 1993 *Nonlinear differential equations and dynamical systems*, 3rd edn. Springer-Verlag.
- WILLIS, A.P., SREENIVASAN, B. & GUBBINS, D. 2007 Thermal core-mantle interaction: exploring regimes for ‘locked’ dynamo action. *Phys. Earth Planet. Int.* **165**, 83–92.
- ZHANG, K. 1991 Vascillatory convection in a rotating spherical shell at infinite Prandtl number. *J. Fluid Mech.* **228**, 607–628.

- ZHANG, K. 1992*a* Convection in a rapidly rotating spherical shell at infinite Prandtl number: transition to vacillating flows. *Phys. Earth Planet. Int.* **72**, 236–248.
- ZHANG, K. 1992*b* Spiralling columnar convection in rapidly rotating spherical fluid shells. *J. Fluid Mech.* **236**, 535–556.
- ZHANG, K. & GUBBINS, D. 1992 On convection in the Earth's core driven by lateral temperature variations in the lower mantle. *Geophys. J. Int.* **108**, 247–255.
- ZHANG, K. & GUBBINS, D. 1993 Convection in a rotating spherical fluid shell with an inhomogeneous temperature boundary condition at infinite Prandtl number. *J. Fluid Mech.* **250**, 209–232.
- ZHANG, K. & GUBBINS, D. 1996 Convection in a rotating spherical fluid shell with an inhomogeneous temperature boundary condition at finite Prandtl number. *Phys. Fluids* **8**, 1141–1148.
- ZHANG, K. & LIAO, X. 2004 A new asymptotic method for the analysis of convection in a rapidly rotating sphere. *J. Fluid Mech.* **518**, 319–346.
- ZHANG, K., LIAO, X. & BUSSE, F.H. 2007 Asymptotic solutions of convection in rapidly rotating non-slip spheres. *J. Fluid Mech.* **578**, 371–380.